

Phonon-mediated third-harmonic generation in diamond

Jiaoyang Zheng^{1D},¹ Guru Khalsa,^{2,3,*} and Jeffrey Moses^{1D},[†]

¹*School of Applied and Engineering Physics, Cornell University, Ithaca, New York 14853, USA*

²*Department of Materials Science and Engineering, Cornell University, Ithaca, New York 14853, USA*

³*Department of Physics, University of North Texas, Denton, Texas 76203, USA*

(Received 29 August 2023; revised 21 June 2024; accepted 2 July 2024; published 25 July 2024)

We observe strongly anisotropic third-harmonic generation mediated by resonant sum-frequency driving of Raman-active phonons with terahertz light, extending light-induced dual control of structural and optical properties in solids. Either strong enhancement or strong suppression of the third harmonic can be achieved, covering six orders of magnitude, a result of interference between purely electronic and phonon-mediated contributions to the polarization field. These findings enrich capabilities for tailoring nonlinear optics via phononics and for the spectroscopy of crystalline structural dynamics.

DOI: 10.1103/PhysRevApplied.22.014066

I. INTRODUCTION

The close connection between structure, symmetry, and function is a principal driver of the search for new quantum materials. Leveraging this connection, prospects for ultrafast control of quantum materials have emerged employing the direct excitation of the crystalline lattice with light. Already, striking changes to functional properties such as superconductivity, magnetism, and ferroelectricity have been achieved through the strong coupling between Raman-active phonons and infrared (IR)-active phonons driven by resonant terahertz laser pulses within the anharmonic regime [1]. Alongside the manipulation of crystal structure, new research has focused on imparting giant changes to the optical properties of crystals through resonant IR-phonon excitation, mediated by the anharmonic lattice potential or nonlinear ionic displacement polarizability [2–5]. The resulting strong optical nonlinearities could have considerable significance for photonics applications involving terahertz light.

However, when IR-active phonons are absent or Raman-IR coupling is weak, alternative strategies for coherent structural and optical property control are imperative. A Raman-active phonon coherence can be driven by two light fields with either a sum-frequency or difference-frequency beat note resonant with the Raman frequency Ω_R . As standard laser frequencies are far higher than phonon frequencies (usually < 50 THz), the difference-frequency pathway, driven by visible or near-IR light fields, is by far the most familiar case in Raman scattering processes. Nonetheless, as strong tabletop terahertz

light sources have advanced, a recent development in crystalline solids is to establish Raman coherence via a sum-frequency beat note of the applied terahertz fields $E(\omega_i)$, a frequency range that avoids electronic heating, where $2\omega_i = \Omega_R$, as Fig. 1(a) shows [6–8]. Using a femtosecond terahertz laser, Maehrlein *et al.* [6] first demonstrated sum-frequency establishment (SFE) of Raman coherence for ultrafast structural modification of diamond. This pathway was corroborated by Johnson *et al.* [7] in cadmium tungstate via two-dimensional terahertz spectroscopy, and by Sato *et al.* [8] in diamond using a free-electron laser.

In addition, Refs. [6–8] discussed two-photon absorption (TPA) of incident terahertz light [Fig. 1(b)] as an inelastic optical scattering effect accompanying SFE of Raman coherence. This stems from a third-order polarizability at the incident frequency, causing nonlinear absorption of terahertz pump at a rate proportional to its intensity [Appendix A, Eq. (A7)]. TPA in this context is analogous to stimulated Raman scattering (SRS), which is an inelastic optical scattering effect that accompanies a *difference-frequency* excitation of a Raman-active phonon. In the case of SRS, optical scattering is incompletely inelastic, with energy transferred from high-frequency to low-frequency photons. In the case of TPA, it is completely inelastic. In both cases, the absorbed optical energy promotes an increase in phonon excited-state population.

In this article, we investigate another strong optical effect associated with SFE of Raman coherence, which was not previously observed in solids: a third-harmonic generation (THG) process enhanced by the intermediate Raman coherence, which we refer to as phonon-mediated (PM) THG [Fig. 1(c)]. We emphasize that the identified effect is present in *all* solids with Raman-active phonons. Just as TPA relates to SRS, PM THG may be regarded

*Contact author: Guru.Khalsa@unt.edu

†Contact author: moses@cornell.edu

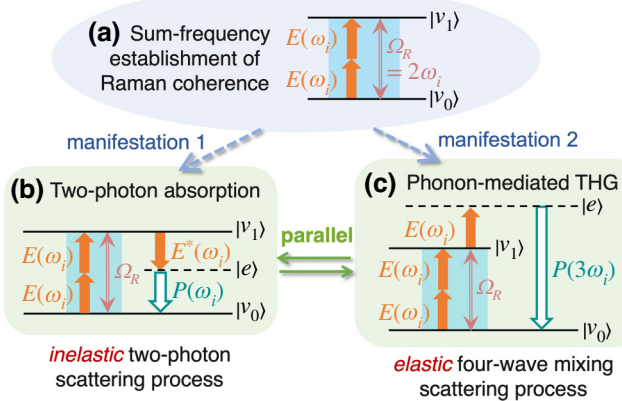


FIG. 1. (a) Sum-frequency pathway for Raman coherence establishment, as described in [6]; (b) its associated *inelastic* two-photon scattering process, TPA, and (c) *elastic* four-wave mixing process, PM THG. Here $|v_0\rangle$ and $|v_1\rangle$ are ground and excited states of a Raman-active phonon, and $|e\rangle$ is a virtual electronic state.

as a low-frequency analog of coherent anti-Stokes Raman scattering (CARS), with Raman coherence established by a sum-frequency pathway rather than the conventional difference-frequency pathway. When the applied fields are degenerate, the “anti-Stokes” frequency, $\omega_a = \omega_i + \Omega_R$, is equivalent to the third harmonic of the incident laser frequency, $3\omega_i$. Like CARS, PM THG is an elastic four-wave mixing process where the Raman coherence increases the optical scattering cross-section but *all incident energy is returned to the optical fields*. Note that TPA and PM THG, as different manifestations of SFE of Raman coherence, are parallel processes that occur simultaneously. (See Appendix A for further comparison and analysis of the four optical scattering effects discussed previously.)

Leveraging the sufficiently narrow bandwidth and high peak intensity of a home-built picosecond terahertz source, we present the first experimental demonstration and theoretical analysis of PM THG in solid-state systems, showcasing attributes distinct from those observed previously in molecular systems [9–13]. Following Refs. [6,8], we study diamond, an important photonic material [14–17] without IR-active phonons. As PM THG in diamond is highly sensitive to field polarization, the contributions of the purely electronic and phonon-mediated pathways to THG near resonance can be disentangled. This allows detection of a remarkable THG enhancement by over 100-fold at resonance that can be further extended to 3000-fold. Moreover, a study of frequency dependence uncovers a new phenomenon, the suppression of THG above resonance due to out-of-phase purely electronic and phonon-mediated contributions to the polarization field, allowing a six-order-of-magnitude tuning range of the THG efficiency. These observations thus illuminate new opportunities for

strongly linked structural and optical property modification of crystals with light at low (terahertz/mid-IR) frequencies. This has relevance both to photonics applications as a strongly enhanced or suppressed solid-state optical wave-mixing nonlinearity, and to condensed-phase physics as a new method for detecting structural dynamics during light-driven material phase control and for spectroscopy in the terahertz regime. We reiterate that in both cases, the relevance is not only to diamond, but to all solids with Raman-active phonons.

II. EXPERIMENTAL SETUP

Our experiment employed an 80- μm -thick type-IIa high-purity diamond crystal plate (nitrogen content < 1 ppm) with [001] orientation grown by microwave plasma chemical vapor deposition (Applied Diamond, Inc.). We focus on the sole Raman-active optical phonon of diamond with F_{2g} symmetry, as investigated in [6,8,18]. We determined the phonon resonant frequency ($f_R = \Omega_R/2\pi = 39.952 \pm 0.002$ THz) and linewidth ($\Gamma/2\pi = 0.056 \pm 0.003$ THz) using a confocal Raman microscope, and found them to be consistent with previous reports [6,18–20] (see Appendix B). To maximize coherent growth of the third-harmonic field, the 80- μm sample thickness was chosen to match the THG coherence length, $L_{coh} = |\pi c / [3\omega_i(n(\omega_i) - n(3\omega_i))]|$, where c is the speed of light and n is the refractive index.

PM THG requires an applied laser frequency f_i at half the phonon frequency, ~ 20 THz. We used a home-built tabletop tunable terahertz source with < 0.5 THz full width at half maximum (FWHM) bandwidth, which is narrower than the pulses used in [6,8]. This bandwidth ensures that a large fraction of the laser power is directed toward Raman-active phonon excitation, which is essential for observing strong PM THG. This terahertz source combines adiabatic difference frequency generation [21,22] with programmable pulse shaping to generate terahertz pulses with customizable bandwidth and central frequency continuously tunable from 14 to 37 THz [23].

A 15-mm focal length ZnSe lens focused the terahertz pump onto the diamond sample, resulting in a maximum fluence of 13 mJ/cm^2 (~ 1 -ps pulse duration and up to 1.5- μJ pulse energy at a 10-kHz repetition rate). Rotation of the diamond plate allowed the electric field of the linearly polarized pump to align parallel to any angle θ in the [100]-[010] crystal plane [Fig. 2(a)]. Emitted light was collimated by a ZnSe lens and passed through two CaF_2 windows to block the terahertz pump before passing into a HgCdTe spectrometer. The terahertz generation stage and the path of the terahertz beam until reaching the diamond plate were purged by N_2 gas to reduce absorption from CO_2 in air.

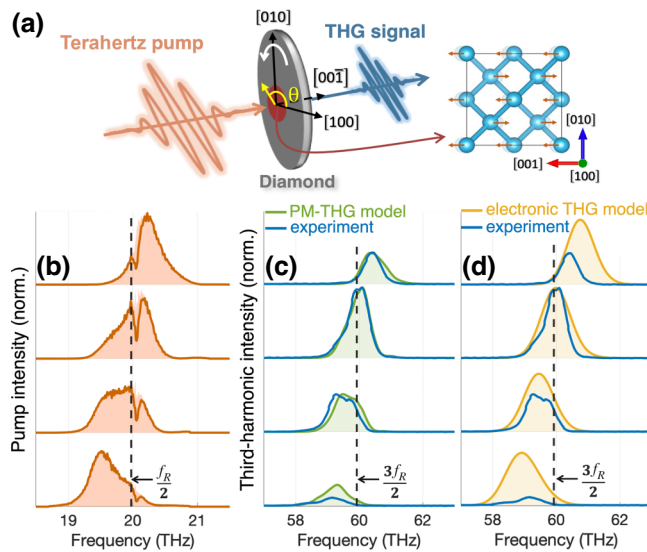


FIG. 2. (a) Orientations of field polarizations, diamond crystal axes, and F_{2g} phonon of diamond. Orange arrows depict the motion of carbon atoms (blue circles) in a phonon oscillation. Measured spectral intensities of (b) terahertz pump and (c),(d) THG signals (blue), compared with theoretical predictions from the PM THG model (green) and electronic THG model (yellow), uniformly normalized across rows such that theoretical and experimental maxima match in the second row.

III. RESULTS

A. Frequency and polarization dependence; THG enhancement factor

We observed a sharp increase in emitted light at the third harmonic of the incident frequency, $3f_i$, and its strong sensitivity to the pump frequency and polarization angle in the vicinity of the resonant condition ($f_i = f_R/2 = 19.98$ THz). Figures 2(b)–2(d) shows the incident pump and emitted third-harmonic spectra, obtained with the crystal plate oriented to maximize the observed THG power. The pump central frequencies were adjusted within a range close to resonance of 19.6–20.4 THz. To corroborate the phonon-mediated origin of the observed THG spectra, we compare them with models based on solely phonon-mediated or purely electronic pathways. For low-frequency fields in diamond, the third-order electric polarization has two components at lowest order,

$$\begin{aligned} P^{(3)}(t) &= \chi_e^{(3)} E(t) E(t) E(t) + \Pi Q_R(t) E(t) \\ &\equiv P_e^{(3)}(t) + P_R^{(3)}(t). \end{aligned} \quad (1)$$

The first term $P_e^{(3)}(t)$ is the origin of nonresonant electronic THG, where $\chi_e^{(3)}$ is the approximately instantaneous third-order electronic susceptibility arising from the anharmonic electronic potential. The second term, $P_R^{(3)}(t)$, is the product of the incident electric field $E(t)$ and the Raman-active

phonon displacement $Q_R(t)$, describing the origin of PM THG. The phonon dynamics can be modeled as a classical Lorentzian oscillator with equation of motion

$$M(\ddot{Q}_R + 2\Gamma\dot{Q}_R + \Omega_R^2 Q_R) = \Pi_{\alpha\beta} E_\alpha E_\beta, \quad (2)$$

where M is the phonon effective mass. The phonon-to-electric-field coupling originates from the dependence of the linear electronic susceptibility $\chi_e^{(1)}$ on Q_R , given by the Raman polarizability tensor Π . For pump field propagating along the diamond [001] axis and polarized at an angle θ , such that $\tilde{E}(t) = E(t) [\cos\theta \sin\theta 0]$ with $\theta = 0^\circ$ corresponding to the [100] direction, this second-rank tensor takes the form [19], $\Pi = \partial\chi_e^{(1)}/\partial Q_R|_{Q_R=0} = \Pi_0 \begin{pmatrix} 0 & 1 & 0 \\ 1 & 0 & 0 \\ 0 & 0 & 0 \end{pmatrix}$.

We solve Eqs. (1) and (2) in the frequency domain and derive the Fourier transforms of $P_e^{(3)}(t)$ and $P_R^{(3)}(t)$ when $E(t)$ is polarized along the [110] axis (see Appendices D and E for full analysis):

$$\tilde{P}_e^{(3)}(\omega) = [\chi_e^{(3)} (\tilde{E}(\omega) * \tilde{E}(\omega))] * \tilde{E}(\omega), \quad (3)$$

$$\begin{aligned} \tilde{P}_R^{(3)}(\omega) &= \Pi_0 \tilde{Q}_R(\omega) * \tilde{E}(\omega) \\ &= [\chi_R^{(3)}(\omega) (\tilde{E}(\omega) * \tilde{E}(\omega))] * \tilde{E}(\omega). \end{aligned} \quad (4)$$

Here $\tilde{E}(\omega)$ and $\tilde{Q}_R(\omega)$ are the Fourier transforms of $E(t)$ and $Q(t)$, and $*$ denotes linear convolution. We defined a Raman susceptibility in Eq. (4),

$$\chi_R^{(3)}(\omega) \frac{\Pi_0^2}{M(\Omega_R^2 - \omega^2 - 2i\Gamma\omega)}. \quad (5)$$

To compare the measurements against theory, we incorporated the pump spectra [Fig. 2(b)] into our theoretical model, and calculated signal spectra corresponding to the PM THG [Fig. 2(c), green] and electronic THG [Fig. 2(d), yellow] mechanisms acting independently. (We note a consistent dip at 20.1 THz in pump spectra resulted from CO₂ absorption along the spectrometer measurement path that was impractical to purge with N₂. To remove this artefact, a Lorentzian absorption model was used to estimate the true pump spectrum at the diamond crystal [Fig. 2(b), shaded region].) While the PM THG model reproduces both the experimental trend in signal intensity and spectral shape, the electronic THG model predicts a signal intensity lacking sensitivity to pump frequency and a broader signal spectrum centered further from resonance than the measurement. The differences between the theoretical predictions can be understood through the form of the nonlinear polarization (Eq. (3) versus Eq. (4)), whereby PM THG contains an implicit convolution between the frequency-dependent Raman coherence $\tilde{Q}_R(\omega)$ and $\tilde{E}(\omega)$, but purely electronic THG involves only a double autoconvolution of $\tilde{E}(\omega)$.

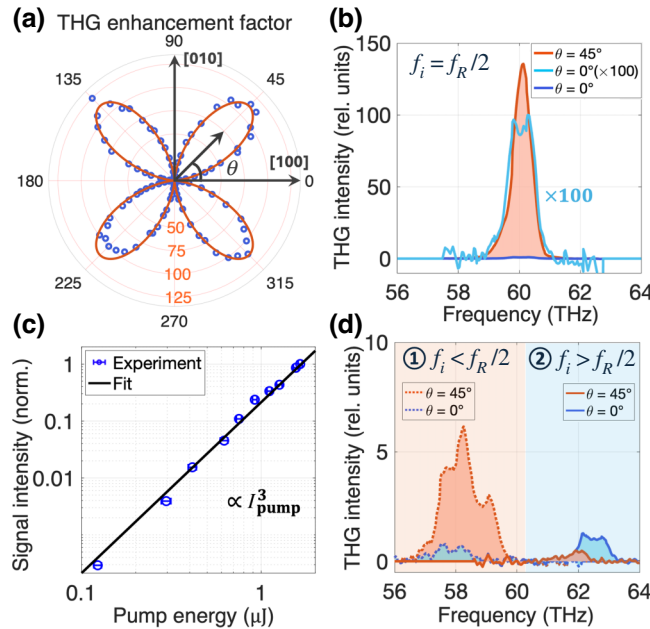


FIG. 3. (a) Polar plot of the THG power enhancement factor (blue circles) versus pump polarization angle θ with pump centered at resonance, with best fit to $113 \sin^2(2\theta)$ (red curve). (b) THG signal spectra observed at $\theta = 45^\circ$ (red) and 0° (dark blue for actual intensity, light blue for intensity magnified by 100). (c) Signal intensity dependence on pump energy at $\theta = 45^\circ$ (log-log scale), with a black line of slope 3 for reference. (d) THG signal spectra observed at $\theta = 45^\circ$ and 0° for pump frequencies below (dotted lines) and above (solid lines) resonance, with corresponding pump spectra shown in Fig. 8. All the signal spectra in (b),(d) are normalized to the maximum signal intensity at $\theta = 0^\circ$ in (b).

Next, by investigating the dependence of the THG power (integrated power spectrum) on pump polarization angle θ , we can both distinguish the relative contributions of the purely electronic and phonon-mediated pathways and reveal interference effects in the total third-order polarization. Figure 3(a) summarizes THG power dependence on pump polarization with the pump frequency f_i centered at the $f_R/2$ resonance. The radial coordinate represents the ratio of third-harmonic signal power to the average of its minima found at $\theta = 0^\circ, 90^\circ, 180^\circ$, and 270° . Strong maxima, exceeding 100, are observed at $\theta = 45^\circ, 135^\circ, 225^\circ$, and 315° . Figure 3(b) compares the signal spectra at $\theta = 45^\circ$ and 0° . Following the theoretical discussion above, the amplitude of Raman oscillation $Q_R \propto \sin(2\theta)$. As the experimental data in Fig. 3(a) is observed to fit closely to a $\sin^2(2\theta)$ function (red curve), we can thus infer that the signal intensity is dominated by the phonon-mediated contribution to the third-order polarizability, $|P^{(3)}|^2 \propto |Q_R|^2$. The nonresonant electronic contribution, in contrast, exhibits near- θ -independence, as determined by the $\chi_e^{(3)}$ tensor of diamond crystal [24] (see Appendix C). Thus, the minimal signal observed at $\theta = 0^\circ$

and 90° originates only from the purely electronic pathway, allowing interpretation of the data in Fig. 3(a) as a THG “enhancement factor” relative to the purely electronic effect. A best fit of $113 \sin^2(2\theta)$ to these data indicates that the phonon-mediated pathway enhances THG intensity by at least a factor of 113.

Figure 3(c) shows the dependence of the third-harmonic signal intensity on incident pump energy at $\theta = 45^\circ$. On a log-log scale, the data fit well to a line of slope 3, confirming a THG process as the signal origin and indicating a largely undiminished terahertz pump and unsaturated phonon oscillation amplitude. This allows interpretation of the measured THG enhancement factor as $|(P_R^{(3)} + P_e^{(3)})/P_e^{(3)}|^2$, from which we deduce a susceptibility ratio at resonance $|\chi_R^{(3)}(\Omega_R)/\chi_e^{(3)}| \gtrsim 58$ (see Appendix D).

B. Interplay between electronic and phonon-mediated responses: observation of THG suppression and conditions for maximum enhancement

Figures 3(a) and 3(b) demonstrate the dominance of the PM THG pathway with a resonant pump. However, detuning the pump frequency reveals a more complex THG phenomenon. As Fig. 3(d) shows, for a pump with central frequency $f_i < f_R/2$, the THG intensity observed at $\theta = 45^\circ$ exceeds that at $\theta = 0^\circ$ by only a factor of 10, a magnitude smaller than the enhancement observed at resonance. Remarkably, for pump central frequency $f_i > f_R/2$, the THG intensity at $\theta = 45^\circ$ is suppressed below that at $\theta = 0^\circ$. This indicates destructive interference between the phonon-mediated and electronic pathways, resulting in a total THG intensity lower than that from the purely electronic contribution alone.

To further explore the possibility of strongly enhanced or suppressed THG, we calculate the THG enhancement factor, $|(P_R^{(3)} + P_e^{(3)})/P_e^{(3)}|^2$, for different pump central frequencies and bandwidths (FWHM), using Eqs. (3), (4) and the obtained susceptibility ratio ($|\chi_R^{(3)}(\Omega_R)/\chi_e^{(3)}| = 58$).

From the results shown in Fig. 4(a), we observe several notable features. First, on resonance ($f_i = f_R/2$), a much larger enhancement is possible than in our experiment. Our experimental pump bandwidth (marked by the vertical dashed line) was ~ 7 –8 times wider than the Raman mode linewidth Γ , resulting in an enhancement factor > 100 on resonance. However, for pump bandwidths narrower than 2.5Γ (corresponding to FWHM pulse durations > 3.2 ps, potentially achievable leveraging chirped-pulse difference-frequency generation (DFG) [25] or DFG quantum cascade lasers [26]), the enhancement factor can surpass 10^3 . This demonstrates the remarkable potential of lattice vibrations to modify the optical properties of crystals. In contrast, for a broader pump bandwidth of 60Γ (corresponding to 130-fs FWHM pulse duration, as used in [6]), the predicted enhancement factor falls to ~ 5 .

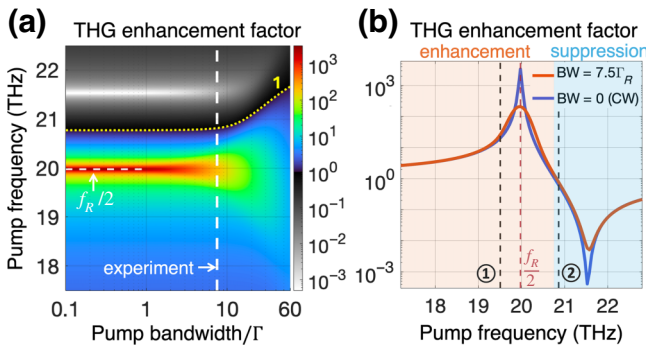


FIG. 4. (a) THG enhancement factor as a function of pump central frequency and bandwidth, spanning from $> 10^3$ to $< 10^{-3}$. The yellow dotted contour line (enhancement factor = 1) divides the figure into two regions: THG enhancement (below) and suppression (above). (b) THG enhancement factor versus pump central frequency for a continuous-wave (CW) pump (blue) and a Gaussian-shaped pump with a bandwidth of $7.5\Gamma_R$ (red), simulating our experimental conditions. Red and blue shading indicates THG enhancement and suppression regions, respectively. Black dashed lines mark pump central frequencies corresponding to the signal ① and ② in Fig. 3(d).

Second, while the THG enhancement factor drops rapidly as the pump central frequency deviates from resonance ($f_R/2$) as expected, this decline is faster with frequency detuning above $f_R/2$ than below it, eventually reaching a region with enhancement factor < 1 . A yellow dotted contour line, denoting a factor of 1, thus divides Fig. 4(a) into two regions: THG enhancement (below) and suppression (above). This trend is further illustrated by Fig. 4(b), showing the frequency-dependent enhancement factor for a continuous-wave (CW) pump and a pump with a bandwidth of 7.5Γ , which simulates our experimental conditions. Suppression occurs when the pump central frequency is detuned beyond 20.8 THz. The pump frequencies corresponding to the signal shown in Fig. 3(d), marked by lines ① and ②, lie within the regions of enhancement (red shading) and suppression (blue shading), respectively. For a pump bandwidth significantly narrower than the Raman linewidth, the total THG intensity can be suppressed to below 10^{-3} times that of the purely electronic pathway at a pump frequency of ~ 21.5 THz. This nearly full cancellation of the nonlinear polarization fields contributed by the phonon-mediated and electronic pathways is explained by the opposite signs of $\chi_e^{(3)}$ and the real part of $\chi_R^{(3)}(\omega)$ above resonance (see Appendix E). Similar interference behavior has been observed between purely electronic and CARS pathways for four-wave mixing between visible frequency waves in diamond [20]. Our first demonstration of this phenomenon in THG thus illustrates the correspondence between optical scattering physics in the terahertz domain via SFE of Raman coherence and

those via traditional difference-frequency excitation with high-frequency light.

IV. CONCLUSION AND OUTLOOK

In summary, we have demonstrated strong anisotropic THG in diamond mediated by resonant sum-frequency driving of Raman-active phonons with terahertz light. The observed pump frequency and polarization dependence of the signal confirm the dominant role of PM THG over purely electronic THG at half the Raman resonance. This polarization dependence, unique to condensed systems, allows the phonon-mediated and purely electronic contributions to be resolved. At resonance, we observed over 100-fold enhancement in THG efficiency, and predict over 3000-fold enhancement for narrower-bandwidth pumping. This corresponds to a nonlinear susceptibility of PM THG surpassing that of purely electronic THG by over 58 times at resonance. Moreover, we have discovered THG suppression above resonance, a result of destructive interference between phonon-mediated and purely electronic contributions to the polarization field. These findings highlight the intimate tie between the nonlinear optical response and the structural response in solids, with timely relevance to several fields of research.

From a photonics perspective, PM THG adds new capabilities to materials platforms through the large enhancement and control of optical coefficients enabled by Raman-active phonons. The strong dependence of the THG efficiency on pump polarization direction and frequency (> 6 orders of magnitude) suggests new applications in areas such as IR nonlinear optical switching and orientation diagnostics. The phonon-mediated pathway may also allow higher-order (e.g., fifth, seventh, or ninth) harmonic generation processes to become efficient, potentially bridging the incident field near 20 THz to the telecommunications range. Requiring only a Raman-active phonon, PM THG is of potential use to any condensed-phase photonics platform. As a degenerate low-frequency analog of CARS, PM THG can also be used for spectroscopic applications amenable to terahertz and mid-IR light, with the unprecedented simplicity of requiring only a single incident frequency compared with stimulated Raman spectroscopies, while sharing CARS' advantage of producing a signal at a frequency distinct from the incident light, thus easing detection. Beyond PM THG, nondegenerate instances of phonon-mediated four-wave mixing could be employed. For example, applying two terahertz frequencies with a sum-frequency beat note slightly detuned from Ω_R might induce significant cross-phase modulation, markedly affecting the refractive indices of the incident fields.

Of significance to the light-driven structural control of quantum materials, our report clarifies that PM THG and TPA are parallel optical polarization effects, elastic and

inelastic, respectively, that both accompany terahertz sum-frequency driving of Raman-active phonons in crystals. Our findings demonstrate the potential of Raman-active phonons to induce marked changes in the optical properties of solids, complementing recent investigations on the changes tied to IR-active phonon nonlinearities [2–5]. Moreover, the duality of structural and optical responses in materials allows PM THG to serve as a convenient marker of concurrent structural changes during light-driven phase transitions. In future work, in analogy to time-domain anti-Stokes Raman scattering [8], the temporal evolution of the coherent phonon amplitude might be resolved by applying a pump and time-delayed probe at the same frequency of $f_R/2$ with a small angular separation, and detecting the resulting noncollinear PM THG signal. This technique eliminates the requirement for carrier-envelope-phase stable terahertz pump pulses. Thus, beyond its value as a strong nonlinear optical response, PM THG offers a powerful laser-lab-scale diagnostic for the growing field of light-driven structural control in condensed matter physics.

The supporting data for this article are openly available from Ref. [27].

ACKNOWLEDGMENTS

This research was primarily supported through the Cornell University Materials Research Science and Engineering Center DMR-1719875. Support for instrumentation was provided by the Kavli Institute at Cornell. The authors thank Ankit Disa and Sören Buchenau for helpful discussions.

APPENDIX A: DERIVATION OF PM THG, TPA, CARS, AND SRS

When the pump field \vec{E} is polarized along $\theta = 45^\circ$ (the [110] axis of crystal), the phonon-mediated third-order polarization, $\vec{P}_R^{(3)}$, as defined in Eq. (1) of the main text, is parallel to \vec{E} (refer to Appendix C for detailed analysis of polarization direction dependence). Therefore, in this section, we write \vec{E} and $\vec{P}_R^{(3)}$ in scalar form to simplify the analysis,

$$P_R^{(3)}(t) = \Pi_0 Q_R(t) E(t). \quad (\text{A1})$$

We assume that $E(t)$ is monochromatic light in the terahertz range with frequency $\omega_i = \Omega_R/2$, $E(t) = E(\omega_i)e^{-i\omega_i t} + c.c.$. The Raman-active phonon Q_R is driven by two force terms with the sum-beat and difference-beat frequencies of the pump field, respectively:

$$\begin{aligned} M(\ddot{Q}_R + 2\Gamma\dot{Q}_R + \Omega_R^2 Q_R) &= \Pi_0 E(t) E(t) \\ &= \Pi_0 (E^2(\omega_i)e^{-i2\omega_i t} + |E(\omega_i)|^2 + c.c.). \end{aligned} \quad (\text{A2})$$

The first term, with a frequency of $2\omega_i = \Omega_R$, resonantly drives the Raman-active phonons. The second term represents a unidirectional force driving at zero frequency, which can be disregarded here due to its contribution being overshadowed by the resonant term. Therefore, the steady-state solution of Eq. (A2) is $Q_R(t) = Q_R(2\omega_i)e^{-i2\omega_i t} + c.c.$, where

$$Q_R(2\omega_i) = \frac{\Pi_0}{M [\Omega_R^2 - (2\omega_i)^2 - 2i\Gamma(2\omega_i)]} E^2(\omega_i). \quad (\text{A3})$$

By substituting Q_R into Eq. (A1), we obtain two frequency components of $P_R^{(3)}(t)$, one at $3\omega_i$ and the other at the pump frequency, ω_i :

$$\begin{aligned} P_R^{(3)}(t) &= P_R^{(3)}(3\omega_i; \omega_i, \omega_i, \omega_i) e^{-i3\omega_i t} \\ &\quad + P_R^{(3)}(\omega_i; \omega_i, \omega_i, -\omega_i) e^{-i\omega_i t} + c.c., \end{aligned} \quad (\text{A4})$$

where

$$\begin{aligned} P_R^{(3)}(3\omega_i; \omega_i, \omega_i, \omega_i) &= \Pi_0 Q_R(2\omega_i) E(\omega_i) \\ &= \chi_R^{(3)}(2\omega_i \simeq \Omega_R) E(\omega_i) E(\omega_i) E(\omega_i) \end{aligned} \quad (\text{A5})$$

represents the origin of PM THG, with the Raman susceptibility given by

$$\chi_R^{(3)}(2\omega_i \simeq \Omega_R) = \frac{\Pi_0^2}{M [\Omega_R^2 - (2\omega_i)^2 - 2i\Gamma(2\omega_i)]}. \quad (\text{A6})$$

The other polarization term at the incident frequency is

$$\begin{aligned} P_R^{(3)}(\omega_i; \omega_i, \omega_i, -\omega_i) &= \Pi_0 Q_R(2\omega_i) E^*(\omega_i) \\ &= \chi_R^{(3)}(2\omega_i \simeq \Omega_R) |E(\omega_i)|^2 E(\omega_i), \end{aligned} \quad (\text{A7})$$

which leads to a TPA process because $\chi_R^{(3)}(2\omega_i \simeq \Omega_R)$ is a pure positive imaginary at the Raman resonance (see Fig. 9). Therefore, the pump field $E(t)$ experiences a non-linear absorption at a rate proportional to its intensity $|E(\omega_i)|^2$.

The above model can also be applied to analyze SRS and CARS, both of which require two high-frequency laser beams usually in the visible or near-IR range, a pump beam $E(\omega_p)e^{-i\omega_p t} + c.c.$ and a Stokes beam $E(\omega_s)e^{-i\omega_s t} + c.c.$ with $\omega_s = \omega_p - \Omega_R$. The Raman-active phonon is resonantly driven by the difference-beat frequency, such that

$Q_R(t) = Q_R(\omega_p - \omega_s)e^{-i(\omega_p - \omega_s)t} + c.c.$, where

$$\begin{aligned} & Q_R(\omega_p - \omega_s) \\ &= \frac{\Pi_0}{M [\Omega_R^2 - (\omega_p - \omega_s)^2 - 2i\Gamma(\omega_p - \omega_s)]} E(\omega_p) E^*(\omega_s). \end{aligned} \quad (\text{A8})$$

Substituting $Q_R(t)$ into Eq. (A1), we derive one third-order polarization term at the anti-Stokes frequency $\omega_a = \omega_p + \Omega_R$, and another at the Stokes frequency ω_s :

$$\begin{aligned} P_R^{(3)}(\omega_a; \omega_p, -\omega_s, \omega_p) \\ = \Pi_0 Q_R(\omega_p - \omega_s) E(\omega_p) \\ = \chi_R^{(3)}(\omega_p - \omega_s \simeq \Omega_R) E^2(\omega_p) E^*(\omega_s), \end{aligned} \quad (\text{A9})$$

which describes the origin of CARS, with

$$\chi_R^{(3)}(\omega_p - \omega_s) = \frac{\Pi_0^2}{M [\Omega_R^2 - (\omega_p - \omega_s)^2 - 2i\Gamma(\omega_p - \omega_s)]}. \quad (\text{A10})$$

Compared with Eq. (A5), both CARS and PM THG involve driving Raman-active phonon coherence as an intermediate step, albeit through different routes: the former via a difference-frequency pathway and the latter via a sum-frequency pathway. As Fig. 5 shows, CARS and

PM THG are both elastic four-wave mixing (FWM) processes, where the Raman coherence increases the optical scattering cross-section but all incident energy is returned to the optical fields. Therefore, we regard PM THG as a low-frequency, single-laser-excitation variant of CARS.

The nonlinear polarization term at the Stokes frequency is

$$\begin{aligned} & P_R^{(3)}(\omega_s; -\omega_p, \omega_s, \omega_p) \\ &= \Pi_0 Q_R(-\omega_p + \omega_s) E(\omega_p) \\ &= \chi_R^{(3)}(-\omega_p + \omega_s \simeq -\Omega_R) |E(\omega_p)|^2 E(\omega_s), \end{aligned} \quad (\text{A11})$$

which represents the origin of SRS. The corresponding Raman susceptibility, $\chi_R^{(3)}(-\omega_p + \omega_s \simeq -\Omega_R)$, is negative imaginary, suggesting an exponential growth of the Stokes field at a rate proportional to the pump intensity $|E(\omega_p)|^2$ [28]. Similar to TPA [Eq. (A7)], optical field energy is absorbed to drive lattice vibrations, and thus not conserved in SRS. Therefore, as illustrated in Figs. 5(a) and 5(c), SRS and TPA are inelastic optical processes that accompany Raman coherence establishment via difference-frequency and sum-frequency pathway, respectively. Phase matching is automatically fulfilled in these two processes.

The relationships and features of the four processes (PM THG, TPA, CARS, and SRS) are summarized in Fig. 5 and Table I.

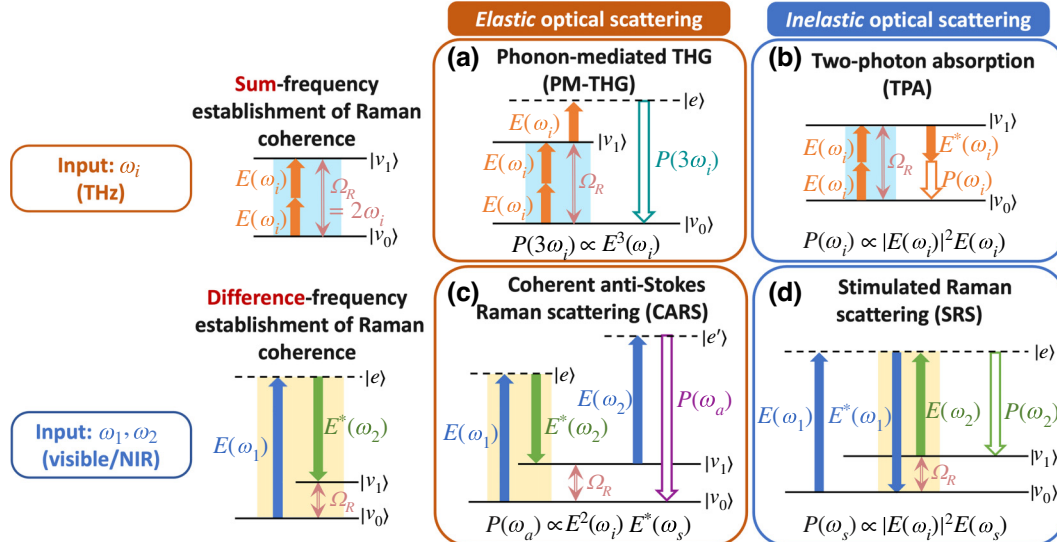


FIG. 5. Comparison of Raman coherence establishment and associated optical effects via sum-frequency and difference-frequency pathways. Top row: Sum-frequency driving of Raman coherence using a single terahertz incident field at $\omega_i = \Omega_R/2$, leading to (a) an elastic optical scattering effect, PM THG, and (b) an inelastic optical scattering effect, TPA. Bottom row: Conventional difference-frequency driving of Raman coherence using two high-frequency light fields at ω_1 and $\omega_2 = \omega_1 - \Omega_R$, resulting in (c) an elastic optical scattering effect, CARS, and (d) an inelastic optical scattering effect, SRS. Here $|v_0\rangle$ and $|v_1\rangle$ are ground and excited states of a Raman-active phonon and $|e\rangle$ and $|e'\rangle$ are virtual electronic excited states.

TABLE I. Summary of characteristics of PM THG, TPA, CARS, and SRS.

Effect	Input beam	Frequency range	Sum/Difference-frequency pathway	Elastic/inelastic	Third-order polarization term
PM THG	ω_i	Terahertz ($\approx \Omega_R/2$)	Sum	Elastic	$P_R^{(3)}(3\omega_i) = \chi_R^{(3)}(2\omega_i \simeq \Omega_R) E^3(\omega_i)$
TPA	ω_i	Terahertz ($\approx \Omega_R/2$)	Sum	Inelastic	$P_R^{(3)}(\omega_i) = \chi_R^{(3)}(2\omega_i \simeq \Omega_R) E(\omega_i) ^2 E(\omega_i)$
CARS	ω_p, ω_s	Visible/near-IR ($\gg \Omega_R$)	Difference	Elastic	$P_R^{(3)}(\omega_a) = \chi_R^{(3)}(\omega_p - \omega_s \simeq \Omega_R) E^2(\omega_p) E^*(\omega_s)$
SRS	ω_p, ω_s	Visible/near-IR ($\gg \Omega_R$)	Difference	Inelastic	$P_R^{(3)}(\omega_s) = \chi_R^{(3)}(-\omega_p + \omega_s \simeq -\Omega_R) E(\omega_p) ^2 E(\omega_s)$

APPENDIX B: RAMAN MICROSCOPY MEASUREMENTS

Figure 6 shows the spectral intensity of the spontaneous Raman signal generated from the diamond sample. This signal was acquired through transmission measurements using a WITec Alpha300R confocal Raman microscope equipped with a CW laser operating at a 532 nm wavelength.

From Ref. [28], the evolution of the Raman signal amplitude $A_s(\omega_s, z)$ propagating along the z -axis (the [001] axis of crystal) is

$$\frac{dA_s(\omega_s, z)}{dz} = -\alpha(\omega_s) A_s(\omega_s, z) \quad (\text{B1})$$

within the slowly varying amplitude approximation. Here, z is the propagation distance, and ω_s represents the Raman signal frequency. We define $\alpha(\omega_s)$ as an absorption coefficient [28],

$$\alpha(\omega_s) = -i \frac{\omega_s}{2\epsilon_0 n(\omega_s) c} \chi_R^{(3)}(-\omega_p + \omega_s) |A_p|^2, \quad (\text{B2})$$

where ϵ_0 is the vacuum permittivity, $n(\omega_s)$ is the linear refractive index, and c is the speed of light. Here A_p

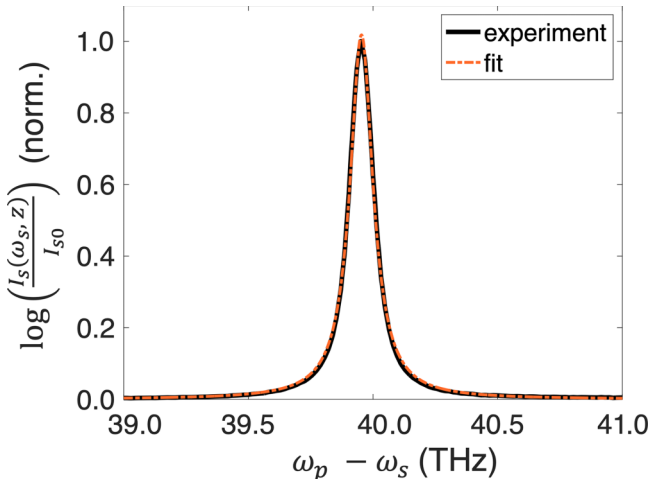


FIG. 6. Measured intensity spectrum of the Raman signal after a log transformation (black) and the fitted curve (orange).

represents the electric field amplitude of the pump at frequency ω_p , which is treated as a constant with no depletion here due to the low efficiency of the spontaneous Raman scattering, and $\chi_R^{(3)}$ is the Raman susceptibility given by Eq. (A10).

The solution of Eq. (B1) is

$$A_s(\omega_s, z) = A_s(\omega_s, 0) e^{-\alpha(\omega_s)z}, \quad (\text{B3})$$

and, thus, the intensity of the Raman signal is

$$I_s(\omega_s, z) = 2\epsilon_0 n(\omega_s) c |A_s(\omega_s, z)|^2 = I_{s0} e^{-2\text{Re}(\alpha(\omega_s))z}. \quad (\text{B4})$$

Since there is only one incident beam at ω_p , the input Raman signal $I_s(\omega_s, z)$ at $z = 0$ arises solely from quantum noise, and thus can be treated as a constant I_{s0} over a narrow frequency band near the Stokes frequency, $\omega_p - \Omega_R$.

After a log transformation, Eq. (B4) becomes

$$\log\left(\frac{I_s(\omega_s, z)}{I_{s0}}\right) = -2\text{Re}(\alpha(\omega_s))z \\ = \beta \text{Re}\left(\frac{i\omega_s}{\Omega_R^2 - (\omega_p - \omega_s)^2 + 2i\Gamma(\omega_p - \omega_s)}\right), \quad (\text{B5})$$

where Ω_R represents the Raman resonant frequency, and Γ is the phonon linewidth [half width at half maximum (HWHM)].

We take the baseline of the measured spectral intensities of the Raman signal (the intensity at frequencies several Γ away from the Stokes frequency) as the value of I_{s0} . β ($\equiv (\Pi_0^2 z / \epsilon_0 n(\omega_s) c M) |A_p|^2$) is a constant to be fitted, where the dispersion of the refractive index $n(\omega_s)$ is neglected.

The black curve in Fig. 6 represents the measured spectral intensities of the Raman signal, $I_s(\omega_s, z)$, after applying the log transformation described previously, and is plotted against the frequency shift $(\omega_p - \omega_s)$. A least-squares fitting of the parameters β , Ω_R , and Γ in Eq. (B5) yields the orange curve, which closely matches the experimental data.

Table II compares our fitted values of $f_R (= \Omega_R/(2\pi))$ and $\gamma (= \Gamma/(2\pi))$ with those reported in the literature for

TABLE II. Resonant frequency (f_R) and the HWHM linewidth (γ) for the F_{2g} phonon of diamond, as reported in prior literature and as observed in our experiments. Here * represents the parameters obtained in the frequency domain and $^\circ$ represents the parameters obtained in the time domain, wherein γ is calculated as the phonon decay rate (in units of ps^{-1}) from [6,18,29], divided by 2π .

Parameter	[6] $^\circ$	[19] *	[18] *	[18] $^\circ$	[20] *	[29] $^\circ$	Our results
Resonant frequency f_R (THz)	39.95 ± 0.01	39.95 ± 0.015	39.91	39.84 ± 0.03	39.93	\	39.952 ± 0.002
Linewidth γ (THz)	0.045	0.0495 ± 0.0006	0.023	0.023 ± 0.006	0.031	0.055 ± 0.006	0.056 ± 0.003

the F_{2g} Raman-active phonon in diamond [6,18–20,29]. Our f_R is consistent with previously reported values, while our γ falls on the higher side of a range of reported values that vary by a factor of ~ 2.4 . This variation is expected as the linewidth depends on the crystal quality and preparation.

APPENDIX C: THEORETICAL ANALYSIS OF PUMP POLARIZATION DEPENDENCE OF THG INTENSITY

This section analyzes the pump polarization dependence of the PM THG signal and the pure electronic THG signal by considering the vectorial nature of the pump field \vec{E} and third-order polarization field $\vec{P}^{(3)}$.

Assuming the terahertz pump field, $\vec{E}(t) = \vec{E}(\omega_0)e^{-i\omega_0 t} + c.c.$ with $\omega_0 = \Omega_R/2$, is polarized along the θ direction within the x - y plane of the crystal, such that

$$\vec{E}(\omega_0) = E_0 [\cos \theta \quad \sin \theta \quad 0], \quad (\text{C1})$$

where x , y , and z correspond to the [100], [010], and [001] crystalline axes, respectively, and E_0 represents the electric field amplitude.

From Eq. (1) in the main text, the phonon-mediated contribution to the third-order polarization $\vec{P}^{(3)}$ at frequency of $3\omega_0$ is

$$P_{R,i}^{(3)}(3\omega_0) = \sum_j \Pi_{ij} Q_R E_j(\omega_0). \quad (\text{C2})$$

From Eq. (2) and the tensor form of Raman polarizability Π provided in the main text, the coherent phonon amplitude is

$$\begin{aligned} Q_R &= \frac{1}{M [\Omega_R^2 - (2\omega_0)^2 - 2i\Gamma(2\omega_0)]} \sum_{ij} \Pi_{ij} E_i(\omega_0) E_j(\omega_0) \\ &= \frac{\Pi_0}{M [\Omega_R^2 - (2\omega_0)^2 - 2i\Gamma(2\omega_0)]} E_0^2 \sin(2\theta), \end{aligned} \quad (\text{C3})$$

which has $\sin(2\theta)$ dependence for the pump polarization angle, consistent with the analysis in Ref. [18].

Inserting Eqs. (C1) and (C3) into Eq. (C2), we obtain

$$\vec{P}_R^{(3)}(3\omega_0) = \chi_R^{(3)}(2\omega_0) E_0^3 \sin(2\theta) [\sin \theta \quad \cos \theta \quad 0]. \quad (\text{C4})$$

Therefore, the intensity of PM THG

$$I_R(3\omega_0) \propto \left| \vec{P}_R^{(3)}(3\omega_0) \right|^2 = \left| \chi_R^{(3)}(2\omega_0) \right|^2 |E_0|^6 \sin^2(2\theta), \quad (\text{C5})$$

which manifests as a $\sin^2(2\theta)$ dependency on the pump polarization angle, as the green curve in Fig. 7 shows. Such angle dependence is consistent with the conventional Raman signal generated from the same F_{2g} phonon in a diamond crystal using a visible pump [30], affirming the link between optical scattering physics in the terahertz domain through sum-frequency driving of Raman coherence and those through traditional difference-frequency coherence excitation with high-frequency light.

However, the pure electronic THG has a significantly different θ dependence. From Eq. (1) in the main text, the nonresonant electronic contribution to the third-order polarization $\vec{P}^{(3)}$ at frequency of $3\omega_0$ is

$$P_{e,i}^{(3)}(3\omega_0) = \sum_{jkl} \chi_{e,ijkl}^{(3)} E_j(\omega_0) E_k(\omega_0) E_l(\omega_0). \quad (\text{C6})$$

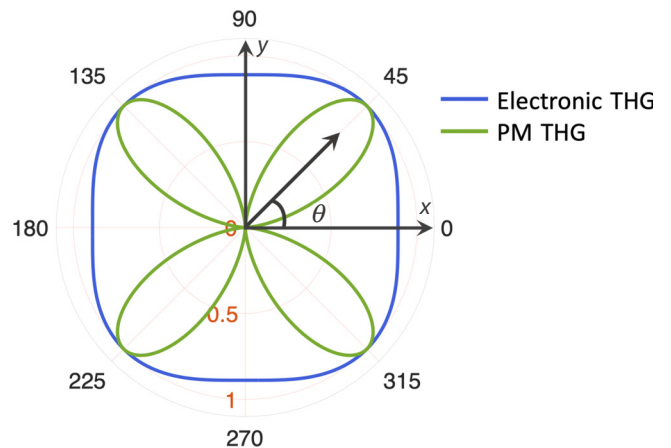


FIG. 7. PM THG (green) and the nonresonant electronic THG (blue) intensities as a function of the pump polarization angle θ , both normalized to their intensity at $\theta = 45^\circ$.

The diamond crystal, belonging to space group No. 227 ($\text{Fd}\bar{3}\text{m}$), has two independent components of $\chi_{e,ijkl}^{(3)}$ dictated by Kleinman's symmetry relation [31]: $\chi_{e,1111}^{(3)}$, and $\chi_{e,1221}^{(3)}$

($= \chi_{e,1212}^{(3)} = \chi_{e,1122}^{(3)}$), where the indices 1 and 2 denote two different Cartesian axes. For example, $\chi_{e,xxxx}^{(3)} = \chi_{e,yyyy}^{(3)} = \chi_{e,1111}^{(3)}$ and $\chi_{e,xyyy}^{(3)} = \chi_{e,yxyx}^{(3)} = \chi_{e,xyyx}^{(3)} = \chi_{e,1221}^{(3)}$. Therefore,

$$P_{e,x}^{(3)}(3\omega_0) = \chi_{e,xxxx}^{(3)} E_x^3(\omega_0) + \left(\chi_{e,xyyx}^{(3)} + \chi_{e,yxyx}^{(3)} + \chi_{e,xyyx}^{(3)} \right) E_y^2(\omega_0) E_x(\omega_0) = \left[\chi_{e,1111}^{(3)} \cos^3(\theta) + 3\chi_{e,1221}^{(3)} \sin^2(\theta) \cos(\theta) \right] E_0^3, \quad (\text{C7})$$

$$P_{e,y}^{(3)}(3\omega_0) = \chi_{e,yyyy}^{(3)} E_y^3(\omega_0) + \left(\chi_{e,yxyx}^{(3)} + \chi_{e,xyyx}^{(3)} + \chi_{e,yyxx}^{(3)} \right) E_x^2(\omega_0) E_y(\omega_0) = \left[\chi_{e,1111}^{(3)} \sin^3(\theta) + 3\chi_{e,1221}^{(3)} \cos^2(\theta) \sin(\theta) \right] E_0^3. \quad (\text{C8})$$

By substituting the susceptibility values from Ref. [24], $\chi_{e,1111}^{(3)} = 4.60$ (10^{-14} esu) and $\chi_{e,1221}^{(3)} = 1.72$ (10^{-14} esu), into Eqs. (C7) and (C8), we calculate the signal intensity of the nonresonant electronic THG, $I_e(3\omega_0) \propto \left| \overrightarrow{P_e^{(3)}}(3\omega_0) \right|^2$, as a function of the polarization angle θ . As the blue curve in Fig. 7 shows, the nonresonant electronic THG is notably less sensitive to the pump polarization angle, with an only 1.12-fold difference between its maximum and minimum intensity.

APPENDIX D: PM THG AND ELECTRONIC THG: DERIVATION FOR PICOSECOND PULSE EXCITATION AND SUSCEPTIBILITY RATIO CALCULATION

To simplify the analysis, we assumed the terahertz pump field $E(t)$ to be monochromatic light in Appendices A and C. While this approach sufficiently illustrates the resonant behavior of PM THG and its dependency on pump polarization angle, it cannot be applied to simulate the THG spectral intensity under excitation of an picosecond laser pump possessing a broad bandwidth. Furthermore, the susceptibility ratio $\left| \chi_R^{(3)}(\Omega_R) / \chi_e^{(3)} \right|$ cannot be simply determined by the ratio between the square root of the THG signal intensity measured at $\theta = 45^\circ$ and that at $\theta = 0^\circ$. Its calculation requires a more careful analysis involving the autoconvolution of the Fourier transform of the pulsed laser field $E(t)$,

$$E(t) = \int \tilde{E}(\omega) \exp(-i\omega t) d\omega, \quad (\text{D1})$$

where $\tilde{E}(\omega)$ is the Fourier transform of $E(t)$, and $|\tilde{E}(\omega)|^2$ represents the intensity spectrum of the pump pulse. Again, we consider the pump field \tilde{E} polarized along $\theta = 45^\circ$ in this section, and write \tilde{E} and the third-order polarization $\tilde{P}^{(3)}$ in scalar form to simplify the analysis.

From Eq. (1), the Fourier transform of the pure electronic third-order polarization term $P_e^{(3)}(t)$ and the phonon-mediated polarization term $P_R^{(3)}(t)$ is

$$\tilde{P}_e^{(3)}(\omega) = [\chi_e^{(3)} (\tilde{E}(\omega) * \tilde{E}(\omega))] * \tilde{E}(\omega), \quad (\text{D2})$$

$$\tilde{P}_R^{(3)}(\omega) = \Pi_0 \tilde{Q}_R(\omega) * \tilde{E}(\omega). \quad (\text{D3})$$

In Eq. (D2), the nonresonant third-order electronic susceptibility $\chi_e^{(3)}(\omega)$ is regarded as a constant $\chi_e^{(3)}$ with no dispersion in the terahertz region, because the photon energy is far below the bandgap of diamond (5.5 eV) [20,32].

From Eq. (2), the transform of $Q_R(t)$ is

$$M \left[(-i\omega)^2 \tilde{Q}_R - 2i\Gamma\omega \tilde{Q}_R + \Omega_R^2 \tilde{Q}_R \right] = \Pi_0 \tilde{E} * \tilde{E}, \quad (\text{D4})$$

where $*$ represents linear convolution. The analytical solution of Eq. (D4) is

$$\tilde{Q}_R(\omega) = \frac{\Pi_0}{M(\Omega_R^2 - \omega^2 - 2i\Gamma\omega)} (\tilde{E}(\omega) * \tilde{E}(\omega)). \quad (\text{D5})$$

By substituting $\tilde{Q}_R(\omega)$ into Eq. (D3), we obtain

$$\begin{aligned} \tilde{P}_R^{(3)}(\omega) &= \left[\frac{\Pi_0^2}{M(\Omega_R^2 - \omega^2 - 2i\Gamma\omega)} (\tilde{E} * \tilde{E}) \right] * \tilde{E} \\ &\equiv \left[\chi_R^{(3)}(\omega) (\tilde{E}(\omega) * \tilde{E}(\omega)) \right] * \tilde{E}(\omega), \end{aligned} \quad (\text{D6})$$

where the Raman susceptibility $\chi_R^{(3)}(\omega)$ is given by

$$\begin{aligned} \chi_R^{(3)}(\omega) &= \frac{\Pi_0^2}{M(\Omega_R^2 - \omega^2 - 2i\Gamma\omega)} \\ &= \chi_e^{(3)} \eta \left(\frac{2\Gamma\Omega_R}{\Omega_R^2 - \omega^2 - 2i\Gamma\omega} \right), \end{aligned} \quad (\text{D7})$$

with an introduced constant η , defined as

$$\eta = \frac{\Pi_0^2}{M (2\Gamma\Omega_R) \chi_e^{(3)}}. \quad (\text{D8})$$

By integrating the measured pump spectra shown in Fig. 2(b), alongside the phonon parameters determined in Appendix B, into Eqs. (D2) and (D6), we derive the respective signal spectra for each of the PM THG mechanism ($|\tilde{P}_R^{(3)}(\omega)|^2$) and the pure electronic-THG mechanism ($|\tilde{P}_e^{(3)}(\omega)|^2$), as shown in Figs. 2(c) and 2(d), respectively.

The constant η is introduced in Eq. (D7) since it directly defines the ratio between $|\chi_R^{(3)}(\omega)|$ at the phonon resonance and $|\chi_e^{(3)}|$. By equating the THG enhancement factor of 113 measured at resonance to $|(P_R^{(3)} + P_e^{(3)})/P_e^{(3)}|^2$, we can deduce the value of the constant η and thus the susceptibility ratio:

$$\eta = \left| \frac{\chi_R^{(3)}(\omega = \Omega_R)}{\chi_e^{(3)}} \right| \geq 58. \quad (\text{D9})$$

Due to experimental uncertainty in polarization purity, there may be some phonon-mediated contribution to the measured THG signal at $\theta = 0^\circ$, potentially leading to an underestimation of the actual enhancement factor. Therefore, we incorporate this uncertainty by utilizing the inequality notation in this expression.

The susceptibility ratio we obtained is approximately three times the value of 21(± 3) reported in Ref. [20]. This discrepancy can be attributed to different definitions of nonlinear susceptibility for different nonlinear optical processes. Our study investigates a THG process with a purely electronic susceptibility given by $\chi_e^{(3)}(3\omega_0; \omega_0, \omega_0, \omega_0) = \chi_{e,1111}^{(3)} + 3\chi_{e,1221}^{(3)}$ for a pump field along the [110] direction (see Appendix C). However, Ref. [20] examines a FWM process with a purely electronic susceptibility $\chi_e^{(3)}(2\omega_1 + \omega_2; \omega_1, \omega_1, -\omega_2) = 3(\chi_{e,1111}^{(3)} + 3\chi_{e,1221}^{(3)})$ when two incident light fields at ω_1 and ω_2 are both along the [110] direction. The electronic susceptibility in the FWM process is three times that of the THG process, resulting in a lower susceptibility ratio between $\chi_R^{(3)}$ and $\chi_e^{(3)}$, as reported in Ref. [20]. In addition, our experiment employs a laser in the terahertz range, while the pump source in Ref. [20] operates in the visible range with photon energy closer to the bandgap. Variations in the third-order electronic susceptibility across different frequency ranges [33] may also contribute to the observed difference in susceptibility ratios.

APPENDIX E: THG SUPPRESSION

Figure 8 presents the pump spectra corresponding to the signal spectra shown in Fig. 3(d), ① below and ② above resonance, respectively.

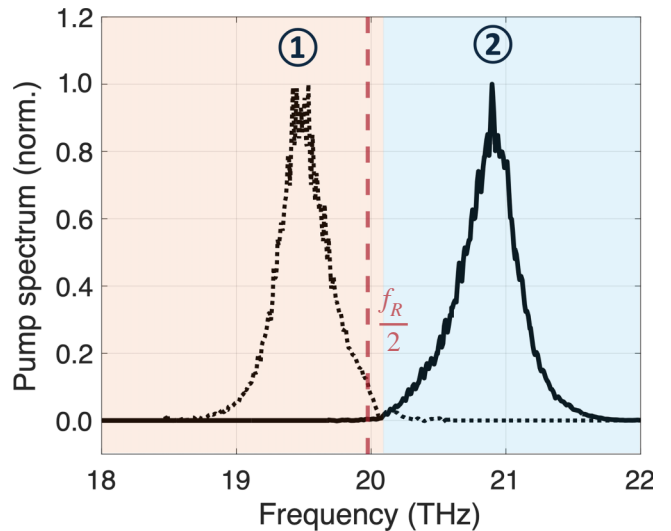


FIG. 8. Pump spectra corresponding to the signal displayed in Fig. 3(d), ① below and ② above half-phonon resonance ($f_R/2$, red dashed line), respectively.

Figure 9 shows the normalized real and imaginary parts of the Raman susceptibility $\chi_R^{(3)}(\omega/2\pi)$ [Eq. (D7)], where $\omega/2\pi$ corresponds to twice the pump central frequency f_i . The normalization is relative to the frequency-independent electronic susceptibility $\chi_e^{(3)}$. When the pump is at half of the phonon resonance ($f_i = f_R/2$), the corresponding Raman susceptibility $\chi_R^{(3)}(\omega/2\pi = f_R)$ is purely imaginary. As f_i deviates from $f_R/2$, $\text{Im}[\chi_R^{(3)}]$ rapidly diminishes to zero, while $\text{Re}[\chi_R^{(3)}]$ becomes dominant in the generation of the PM THG signal. For instance, the central frequency of pump ① in Fig. 8 corresponds to a Raman susceptibility $\chi_R^{(3)}(\omega)$ whose real part is much higher than its imaginary part, marked by a yellow dashed line ① in Fig. 9. As $\chi_e^{(3)}$ is real and shares the same sign as $\text{Re}[\chi_R^{(3)}(\omega)]$, the electronic and phonon-mediated contributions to the third-order polarization field combine constructively, leading to an enhancement of the total THG efficiency, as observed in Fig. 3(d), albeit with a significantly smaller enhancement factor than at resonance.

Conversely, when the pump frequency is tuned above $f_R/2$, $\text{Re}[\chi_R^{(3)}(\omega)]$ flips its sign, leading to destructive interference between the polarization fields of PM THG and electronic THG. Therefore, for pump ② in Fig. 8, whose doubled central frequency is indicated by yellow dashed line ② in Fig. 9, the total THG efficiency is suppressed below that of the purely electronic THG, as experimentally demonstrated in Fig. 3(d). Notably, the THG signal cannot be completely eliminated even with a perfect cancellation between $\chi_e^{(3)}$ and $\text{Re}[\chi_R^{(3)}(\omega)]$, as a result of the minor contribution from $\text{Im}[\chi_R^{(3)}]$. This explains why the minimum enhancement factor, illustrated in Fig. 4(b), is not strictly zero but rather on the order of 10^{-4} .

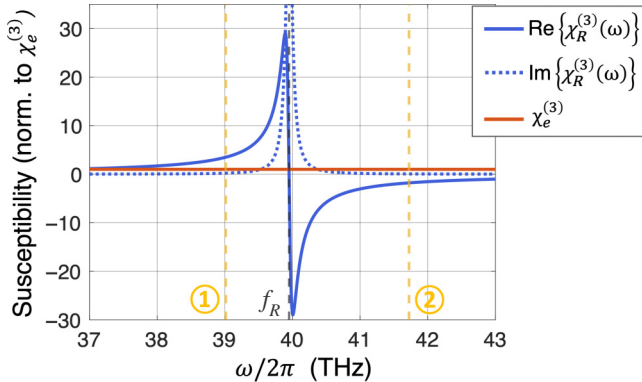


FIG. 9. Third-order susceptibility as a function of frequency ω . Blue curves show the real (solid) and imaginary (dotted) components of the Raman susceptibility $\chi_R^{(3)}$, both normalized to the frequency-independent third-order electronic susceptibility $\chi_e^{(3)}$ (red line). Yellow dashed lines marked by ① and ② indicate twice the central frequencies of pump ① and ② in Fig. 8 respectively.

We note that Ref. [13] detected an asymmetric THG response in HCl vapor, attributed to interference between THG from the sample and the background THG from gas vessel windows. Our findings suggest this may instead be due to the intrinsic interference effect we have observed, which could not be disentangled by adjusting the pump polarization direction in the randomly oriented gas.

- [1] A. S. Disa, T. F. Nova, and A. Cavalleri, Engineering crystal structures with light, *Nat. Phys.* **17**, 1087 (2021).
- [2] K. Dolgaleva, D. V. Materikina, R. W. Boyd, and S. A. Kozlov, Prediction of an extremely large nonlinear refractive index for crystals at terahertz frequencies, *Phys. Rev. A* **92**, 023809 (2015).
- [3] G. Khalsa, N. A. Benedek, and J. Moses, Ultrafast control of material optical properties via the infrared resonant Raman effect, *Phys. Rev. X* **11**, 021067 (2021).
- [4] J. S. Ginsberg, M. M. Jadidi, J. Zhang, C. Y. Chen, N. Tancogne-Dejean, S. H. Chae, G. N. Patwardhan, L. Xian, K. Watanabe, T. Taniguchi, *et al.*, Phonon-enhanced nonlinearities in hexagonal boron nitride, *Nat. Commun.* **14**, 7685 (2023).
- [5] S. Zibod, P. Rasekh, M. Yildrim, W. Cui, R. Bhardwaj, J.-M. Ménard, R. W. Boyd, and K. Dolgaleva, Strong nonlinear response in crystalline quartz at THz frequencies, *Adv. Opt. Mater.* **11**, 2202343 (2023).
- [6] S. Maehrlein, A. Paarmann, M. Wolf, and T. Kampfrath, Terahertz sum-frequency excitation of a Raman-active phonon, *Phys. Rev. Lett.* **119**, 127402 (2017).
- [7] C. L. Johnson, B. E. Knighton, and J. A. Johnson, Distinguishing nonlinear terahertz excitation pathways with two-dimensional spectroscopy, *Phys. Rev. Lett.* **122**, 073901 (2019).
- [8] O. Sato, K. Yoshida, H. Zen, K. Hachiya, T. Goto, T. Sagawa, and H. Ohgaki, Two-photon selective excitation of phonon-mode in diamond using mid-infrared free-electron laser, *Phys. Lett. A* **384**, 126223 (2020).
- [9] C. She and K. W. Billman, Infrared-pumped third-harmonic and sum-frequency generation in diatomic molecules, *Appl. Phys. Lett.* **27**, 76 (1975).
- [10] H. Kildal and T. Deutsch, Infrared third-harmonic generation in molecular gases, *IEEE J. Quantum Electron.* **12**, 429 (1976).
- [11] H. Kildal and S. Brueck, Resonant infrared third-harmonic generation in cryogenic liquids, *Phys. Rev. Lett.* **38**, 347 (1977).
- [12] Y. Miyamoto, H. Hara, T. Hiraki, T. Masuda, N. Sasao, S. Uetake, A. Yoshimi, K. Yoshimura, and M. Yoshimura, Vibrational excitation of hydrogen molecules by two-photon absorption and third-harmonic generation, *J. Phys. B: At. Mol. Opt. Phys.* **51**, 015401 (2017).
- [13] J. F. Kinder, F. Cipura, and T. Halfmann, Detection of HCl molecules by resonantly enhanced third-harmonic generation, driven by midinfrared laser pulses, *Phys. Rev. A* **103**, 052808 (2021).
- [14] I. Aharonovich, A. D. Greentree, and S. Prawer, Diamond photonics, *Nat. Photonics* **5**, 397 (2011).
- [15] B. Hausmann, I. Bulu, V. Venkataraman, P. Deotare, and M. Lončar, Diamond nonlinear photonics, *Nat. Photonics* **8**, 369 (2014).
- [16] E. Janitz, M. K. Bhaskar, and L. Childress, Cavity quantum electrodynamics with color centers in diamond, *Optica* **7**, 1232 (2020).
- [17] A. Abulikemu, Y. Kainuma, T. An, and M. Hase, Second-harmonic generation in bulk diamond based on inversion symmetry breaking by color centers, *ACS Photonics* **8**, 988 (2021).
- [18] K. Ishioka, M. Hase, M. Kitajima, and H. Petek, Coherent optical phonons in diamond, *Appl. Phys. Lett.* **89**, 231916 (2006).
- [19] S. Solin and A. Ramdas, Raman spectrum of diamond, *Phys. Rev. B* **1**, 1687 (1970).
- [20] M. Levenson, C. Flytzanis, and N. Bloembergen, Interference of resonant and nonresonant three-wave mixing in diamond, *Phys. Rev. B* **6**, 3962 (1972).
- [21] H. Suchowski, P. R. Krogen, S.-W. Huang, F. X. Kärtner, and J. Moses, Octave-spanning coherent mid-IR generation via adiabatic difference frequency conversion, *Opt. Express* **21**, 28892 (2013).
- [22] P. Krogen, H. Suchowski, H. Liang, N. Flemens, K.-H. Hong, F. X. Kärtner, and J. Moses, Generation and multi-octave shaping of mid-infrared intense single-cycle pulses, *Nat. Photonics* **11**, 222 (2017).
- [23] W.-Z. Chang, J. Zheng, N. Flemens, D. Heberle, and J. Moses, in *Conference on Lasers and Electro-Optics (CLEO)*, edited by J. Kang *et al.* (Optica Publishing Group, San Jose, CA, USA, 2021), pp. 1–2.
- [24] M. Levenson and N. Bloembergen, Dispersion of the nonlinear optical susceptibility tensor in centrosymmetric media, *Phys. Rev. B* **10**, 4447 (1974).
- [25] A. Cartella, T. F. Nova, A. Oriana, G. Cerullo, M. Först, C. Manzoni, and A. Cavalleri, Narrowband carrier-envelope phase stable mid-infrared pulses at wavelengths beyond

- 10 μm by chirped-pulse difference frequency generation, *Opt. Lett.* **42**, 663 (2017).
- [26] L. Consolino, S. Jung, A. Campa, M. De Regis, S. Pal, J. H. Kim, K. Fujita, A. Ito, M. Hitaka, S. Bartalini, *et al.*, Spectral purity and tunability of terahertz quantum cascade laser sources based on intracavity difference-frequency generation, *Sci. Adv.* **3**, e1603317 (2017).
- [27] Data Repository, <https://doi.org/10.7298/7gn0-q524>.
- [28] R. W. Boyd, *Nonlinear Optics* (Academic press, 2008), pp. 473–509.
- [29] A. Laubereau, D. Von der Linde, and W. Kaiser, Decay time of hot TO phonons in diamond, *Phys. Rev. Lett.* **27**, 802 (1971).
- [30] S. Brown and S. C. Rand, Site symmetry analysis of the 738 nm defect in diamond, *J. Appl. Phys.* **78**, 4069 (1995).
- [31] M. I. Aroyo, J. M. Perez-Mato, D. Orobengoa, E. Tasci, G. de la Flor, and A. Kirov, Crystallography online: Bilbao crystallographic server, *Bulg. Chem. Commun.* **43**, 183 (2011).
- [32] M. Kozák, F. Trojánek, B. Dzurňák, and P. Malý, Two- and three-photon absorption in chemical vapor deposition diamond, *JOSA B* **29**, 1141 (2012).
- [33] J. M. Almeida, C. Oncebay, J. P. Siqueira, S. R. Muniz, L. De Boni, and C. R. Mendonça, Nonlinear optical spectrum of diamond at femtosecond regime, *Sci. Rep.* **7**, 1 (2017).